

Imaging fractures and sedimentary fabrics using shear wave splitting measurements made on passive seismic data

J. P. Verdon, J.-M. Kendall and A. Wüstefeld

Department of Earth Sciences, Wills Memorial Building, University of Bristol, Bristol, BS8 1RJ, UK. E-mail: gljpv@bristol.ac.uk

Accepted 2009 July 25. Received 2009 June 2; in original form 2009 February 12

SUMMARY

The ability to detect aligned fractures using seismic anisotropy provides a valuable tool for exploiting hydrocarbon reservoirs better. Perhaps the most direct way of identifying anisotropy is by observing shear wave splitting. However, the interaction of shear waves with subsurface structure is often complicated. Although fractures in hydrocarbon reservoirs are usually sub-vertical, shear waves recorded on downhole receivers from microseismic events in or near the reservoir are not likely to have travelled vertically. As such, interpreting splitting measurements made on such waves is a non-trivial problem. Here we develop an approach to model the effects of subsurface structure on non-vertically propagating shear waves. Rock physics theory is used to model the effects of sedimentary fabrics as well as fractures, allowing us to use shear wave splitting measurements to invert for aligned fractures. We use synthetic examples to demonstrate how it is possible to assess in advance how well splitting measurements will image structures, and how this is highly dependent on the available range of ray coverage. Finally, we demonstrate the inversion technique on a passive seismic data set collected during hydraulic fracture stimulation. Despite an unfavourable source–receiver geometry, the strike of an aligned fracture set is accurately identified.

Key words: Inverse theory; Downhole methods; Seismic anisotropy; Fractures and faults.

1 INTRODUCTION

Seismic anisotropy refers to the situation where the velocity of a seismic wave is dependent on its direction of propagation and/or polarization. Seismic anisotropy in sedimentary rocks can have many causes, which act at many length-scales. These mechanisms include mineral alignment (e.g. Valcke *et al.* 2006), alignment of grain-scale fabrics (e.g. Hall *et al.* 2008), which can be distorted by non-hydrostatic stresses (e.g. Zatsepin & Crampin 1997; Verdon *et al.* 2008), larger scale sedimentary layering (e.g. Backus 1962) and the presence of aligned fracture sets (e.g. Hudson 1981). In hydrocarbon settings, the most common anisotropic mechanisms are horizontally aligned consisting of a combination of sedimentary layering, grain-scale fabrics and mineral alignment. This creates a vertically transverse anisotropic system (VTI). A second source of anisotropy is often introduced with vertical alignment (horizontal transverse anisotropy, HTI) due to the presence of subvertical fracture sets. The combination of such mechanisms leads to anisotropic systems with orthorhombic or lower symmetry systems. The presence of fractures has a significant impact on permeability and alignment leads to anisotropic permeability. The detection of seismic anisotropy has the potential to image aligned fracture sets, and so can be a useful tool to help guide drilling and production strategies.

Shear wave splitting (SWS) is probably the least ambiguous indicator of seismic anisotropy. As a shear wave enters an anisotropic

region it is split into two orthogonally polarized waves, one of which will travel faster than the other. The polarization of the fast wave (ψ), and the time-lag (δt) between the arrival of the fast and slow waves, characterizes the splitting along a ray path. The splitting along many ray paths characterizes the overall anisotropy symmetry system. Usually, δt is normalized by the path length to give the percentage difference in *S*-wave velocities, δV_S .

In hydrocarbon settings, the shear waves used to measure SWS can come from two very different sources: the first being controlled source multicomponent reflection seismics, the second being microseismic events in and around the reservoir generated by stress changes and recorded on geophones located in boreholes. Seismic waves travel subvertically in reflection seismics. When interpreting the splitting in such situations, ψ is assumed to represent the orientation of a fracture set, with increasing δV_S representing an increase in fracturing. However, this method of interpretation is limited in its validity to situations where the shear waves have propagated subvertically. This is rarely the case when measuring SWS from microseismic events recorded on downhole geophones. Interpretation of SWS then becomes far less intuitive.

From both rock physics theory and observation (see Crampin & Peacock 2008, for a review) we know that ψ and δV_S are highly dependent on the direction of ray propagation with respect to a fracture set. Additionally, other subsurface structures such as sedimentary fabrics can contribute to the overall anisotropy. We argue that any

interpretation of SWS from non-vertically propagating shear waves must be guided by elastic models that consider the range of plausible anisotropy mechanisms in a reservoir setting.

In this paper, we outline an inversion approach that uses rock physics modelling to select the best-fitting fracture geometries and sedimentary fabrics to match SWS observations. We demonstrate our approach using a passive seismic data set collected during a hydraulic fracture stimulation. Previous attempts to invert splitting measurements include Horne & MacBeth (1994), Teanby *et al.* (2004a) and Rial *et al.* (2005). Synthetic tests can provide insight into any inversion technique. The checkerboard test used in seismic velocity tomography is probably the best example of this. Synthetic tests constrain what can and cannot be imaged given the real data available, and can highlight which parameters are the most significant. We develop synthetic examples for our inversion technique in order to test the sensitivity, and show that the success of a SWS inversion is highly dependent on the range of arrival azimuths and inclinations that are available. It is possible, using such techniques, to determine in advance which structures are detectable with SWS, and which are not. It is also possible to identify potential trade-offs between parameters than can affect the accuracy of such inversions. This will be useful not only in assessing the reliability of SWS interpretations, but also potentially in advance when selecting geophone locations for passive seismic monitoring in order to maximize what can be imaged using SWS.

2 METHOD

2.1 Model building using rock physics

In order to model SWS caused by fractures and sedimentary fabrics, we need to construct realistic rock physics models. As we wish to model SWS for waves travelling in any direction, we must have a model that computes the full $3 \times 3 \times 3 \times 3$ stiffness tensor \mathbf{C} (or its inverse, compliance $\mathbf{S} = \mathbf{C}^{-1}$). We use the additional compliance approach of Schoenberg & Sayers (1995), where the compliance of the fractures, $\Delta\mathbf{S}$, is added to the rock frame compliance, \mathbf{S}^r , to give the overall compliance,

$$\mathbf{S} = \mathbf{S}^r + \Delta\mathbf{S}. \quad (1)$$

The rock frame compliance can be anisotropic if horizontal layering is present. Based on previous estimates of sedimentary fabric anisotropy in siliciclastic rocks (Kendall *et al.* 2007) we consider the rock fabric to have VTI symmetry. For such a system, the frame compliance tensor (in contracted Voigt notation) is given by

$$\mathbf{S}^r = \begin{pmatrix} C_{11}^r & (C_{11}^r - 2C_{66}^r) & C_{13}^r & 0 & 0 & 0 \\ (C_{11}^r - 2C_{66}^r) & C_{11}^r & C_{13}^r & 0 & 0 & 0 \\ C_{13}^r & C_{13}^r & C_{33}^r & 0 & 0 & 0 \\ 0 & 0 & 0 & C_{44}^r & 0 & 0 \\ 0 & 0 & 0 & 0 & C_{44}^r & 0 \\ 0 & 0 & 0 & 0 & 0 & C_{66}^r \end{pmatrix}^{-1}, \quad (2)$$

where $C_{11}^r > C_{33}^r$ and $C_{66}^r > C_{44}^r$. The strength of the shear wave anisotropy caused by the VTI system is given by Thomsen's 1986 γ and δ parameters, defined as

$$\gamma = \frac{C_{66}^r - C_{44}^r}{2C_{44}^r} \quad (3)$$

and

$$\delta = \frac{(C_{13}^r + C_{44}^r)^2 - (C_{33}^r - C_{44}^r)^2}{2C_{33}^r(C_{33}^r - C_{44}^r)}. \quad (4)$$

The additional compliance introduced by a set of vertical, aligned fractures in a VTI medium with normals parallel to the x_1 axis ($\mathbf{n} = [1, 0, 0]$) is given by Grechka (2007) as

$$\Delta\mathbf{S} = \begin{pmatrix} B_N & 0 & 0 & 0 & 0 & 0 \\ 0 & 0 & 0 & 0 & 0 & 0 \\ 0 & 0 & 0 & 0 & 0 & 0 \\ 0 & 0 & 0 & 0 & B_{Tv} & 0 \\ 0 & 0 & 0 & 0 & 0 & B_{Th} \end{pmatrix}. \quad (5)$$

B_N is the normal compliance of the fracture, and B_{Th} and B_{Tv} are the shear compliances in the vertical and horizontal planes. Having computed the stiffness tensor for fractures aligned in the $x_2:x_3$ plane we rotate to give the stiffness tensor for fractures with the desired strike. B_{Th} and B_{Tv} will only differ when significant VTI anisotropy is present. Furthermore, we believe that they will only differ when the mechanism causing VTI anisotropy acts at a smaller length-scale than the vertical fractures (e.g. horizontally aligned anisotropic minerals). If the VTI anisotropy is induced by horizontally aligned fractures or by larger scale sedimentary layers (e.g. Backus 1962) then it is not clear that B_{Th} and B_{Tv} should be allowed to differ.

It is possible to calculate the fracture normal and tangential compliance as a function of fracture density, aspect ratio and fill by assuming an idealized fracture geometry (e.g. penny-shaped or elliptical). In this paper, we use the approach outlined by Hudson *et al.* (1996) to compute the normal and tangential compliances of a set of aligned penny shaped cracks set in a matrix containing equant pores. In this model the fracture compliance is frequency dependent. However, in order to simplify the model and reduce the number of free parameters in the inversion, we take the low frequency end-member for this model. This is equivalent to the Hudson (1981) model with unfilled fractures. In this case, B_N , B_{Tv} and B_{Th} are given by

$$B_N = \frac{4}{3} \left(\frac{\xi}{C_{66}^r} \right) \left(\frac{C_{11}^r}{C_{11}^r - C_{66}^r} \right), \quad (6)$$

$$B_{Th} = \frac{16}{3} \left(\frac{\xi}{C_{66}^r} \right) \left(\frac{C_{11}^r}{3C_{11}^r - 2C_{66}^r} \right), \text{ and} \quad (7)$$

$$B_{Tv} = \frac{16}{3} \left(\frac{\xi}{C_{44}^r} \right) \left(\frac{C_{33}^r}{3C_{33}^r - 2C_{44}^r} \right), \quad (8)$$

where ξ is the non-dimensional fracture density. This assumption is appropriate both in that seismic waves generally have low frequencies, and because this enables us to focus on the key first order parameter, ξ , and removes the need to consider other parameters such as fracture aperture and rock permeability, to which SWS is less sensitive. There are a range of models in the literature for computing fracture compliances. The Hudson (1981) model is one of the simplest, yet it has been successfully applied in numerous cases, especially when treated as the low frequency end-member of the Hudson *et al.* (1996) model. Given the quality of data available, we feel that this is the most appropriate model to be used. The interested reader is directed towards Pointer *et al.* (2000) and Hall & Kendall (2000) for reviews and further discussions of the most commonly used fracture models available in the literature.

We now have a set of equations to compute the elastic stiffness of a rock containing a horizontal sedimentary fabric and vertical fractures. The key variables are fracture density, ξ , fracture strike,

α (given in degrees from north), and the VTI fabric strength, given by γ and δ . Effectively, we derive an orthorhombic symmetry, and it is worth noting that *a priori* knowledge of the exact cause of the anisotropy is not required. For example, the VTI component could be caused by inclusions, minerals or microcracks, all of which can show a horizontal preferred alignment.

2.2 Inversion workflow

In order to find the best-fitting rock physics model, we perform a grid search over the free parameters (ξ , α , γ and δ), computing the elastic stiffness tensor in each case. Using ray theory the slowness surface, and hence the speeds and polarizations for propagation in any direction of all three body waves (P , fast and slow S), can be computed by solving the Christoffel equation,

$$(C_{ijkl}p_j p_k - \rho \delta_{il})g_l = 0, \quad (9)$$

where p_i is the i th component of slowness, g_l is the l th component of polarization and ρ is the rock density. A non-trivial solution for the polarization g_l requires

$$\det |a_{ijkl}n_j n_k - v_n^2 \delta_{il}| = 0, \quad (10)$$

where a_{ijkl} is the elastic tensor normalized by ρ , n_i is the wave normal, $p_i v_n$ and v_n is the n th phase velocity. We use the Christoffel equation to compute ψ and δV_S for each arrival azimuth (θ) and inclination (ϕ) that is present in the observed data set. The modelled ψ and δV_S values are compared with the observed values, and the rms misfit computed. The model that minimizes the rms misfit is selected as the most appropriate. Note that in all cases, ψ refers to the fast wave polarization in ray-frame coordinates, there is no rotation into geographical or other coordinate systems as is often done when interpreting SWS. We assume that in all cases splitting

does occur, and that there are no nul results caused by coincidence of a symmetry axis with the initial S -wave polarization (e.g. Wustefeld 2007).

We compute the misfit between ψ and between δV_S separately, and normalize both by their minimum values, before summing them to give the overall misfit. Conceptually, there is no reason why this sum could not be weighted such that fitting either δV_S or ψ was given priority in the inversion (for instance, if one was more accurately known than the other), however, we have no reason to treat them differently in this paper. Having computed the overall misfit, we compute the 90 per cent confidence interval using an F -test (see, for e.g. Silver & Chan 1991, in appendix). The workflow for this process is outlined in Fig. 1.

An assumption implicit in this approach is that all the rock mass through which the shear waves have travelled has similar physical properties. If there is significant spatial variation in the anisotropic system along a single or between different ray paths then this approach may breakdown. Tomographic techniques are being developed that invert for spatial variations in anisotropy (e.g. Abt & Fischer 2008; Wookey 2009). However these tend to run into under-determination problems, where the number of free parameters available (the spatial distribution of each area with differing anisotropy, as well as the anisotropic parameters for each area) serve only to introduce trade-offs and non-uniqueness to the solutions. Where no significant variations are anticipated—as is often the case with reservoir microseismics—our approach has the advantage of ease of application and much reduced computational requirements [the tomographic approach of Wookey (2009) requires a cluster to perform the computations]. In practice, we anticipate that for real cases where significant spatial variation exists our approach would fail to find significant minima. This could be used as an indication that spatial variations are present, and that tomographic techniques are necessary.

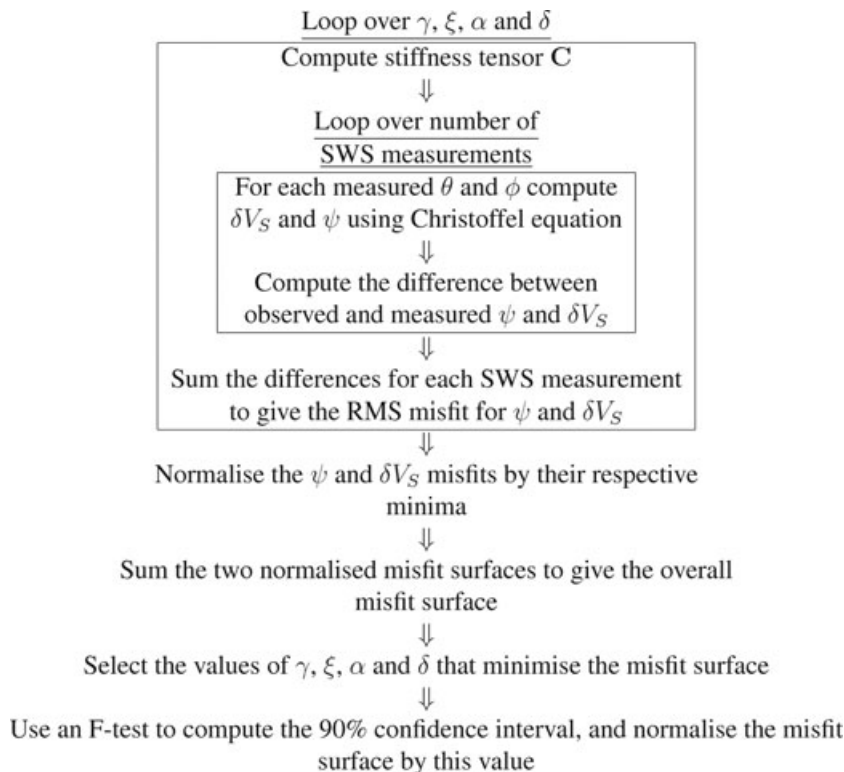


Figure 1. Workflow for inverting for rock physics parameters from SWS measurements.

3 SYNTHETIC TESTING

Before applying this technique to a real data set we use synthetic examples to demonstrate and understand the inversion process better. The first step is the construction of an initial elastic model using the rock physics model outlined above. A range of plausible ray path arrival azimuths and inclinations are chosen. The splitting parameters ψ and δV_S for each ray path are calculated using the Christoffel equation. We apply noise to the data by assuming a random error distribution between $\pm 10^\circ$ for ψ and ± 0.3 per cent for δV_S , which are typical error ranges for real splitting data. This then represents the ‘observed’ data set, which we use to invert for the initial model parameters. The closeness between the initial parameters used to construct the elastic model and those found by the inversion will indicate the success of the inversion. Even where the initial parameters are recovered, we examine the misfit space to assess how well constrained the result is.

3.1 Sensitivity of δ and γ

Our first use of synthetic data is to test the sensitivity of the inversion to γ and δ . We anticipate that this will be highly dependent on the range of ray path inclinations. We perform three inversions, with subhorizontal ($0\text{--}30^\circ$), subvertical ($60\text{--}90^\circ$) and oblique ($30\text{--}60^\circ$) arrivals. In each case there is a full range of arrival azimuths from 0° to 180° , and the initial elastic model has $\gamma = 0.04$, $\delta = 0.1$, $\xi = 0.04$ and $\alpha = 120^\circ$. In Figs 2–4, we plot the rms misfit contours as a function of γ , δ and α , at the best-fitting value of ξ . The rms

misfit is normalized such that a misfit of 1 represents the 90 per cent confidence interval. The initial and best-fitting models are marked.

First we consider the case with subhorizontal arrivals (Fig. 2). Fracture strike and γ are well constrained. However, from the elongation of the misfit contours along the δ axis, we infer that this parameter is not as well constrained, and therefore is not having an influence on the inversion. This is because splitting of subhorizontal shear waves is not significantly affected by the size of δ . For the case with subvertical arrivals (Fig. 3), there is a trade-off in the inversion between δ and γ , meaning that neither is well constrained. For the case with obliquely arriving waves (Fig. 4) there is still some trade-off between γ and δ , though both are better constrained than with the subvertical arrivals. In all the examples the fracture strike and density are both well imaged.

From these inversions we infer that when the arrivals are subhorizontal γ is significant whilst δ can be neglected, whilst for subvertical arrivals neither can be imaged accurately. However, at oblique angles both γ and δ may be imaged.

3.2 Sensitivity with the available data

In the subsequent section, we will analyse SWS data from a real data set. It will be therefore be useful to assess what to expect from the range of θ and ϕ available using synthetic examples. As can be seen in Fig. 5(b), the data is limited to subhorizontal arrivals with a 70° range in azimuth. Given such a limited range of arrivals, can we expect to image fractures, and if so, to identify their strike and density? Note that as we are dealing with subhorizontal arrivals,

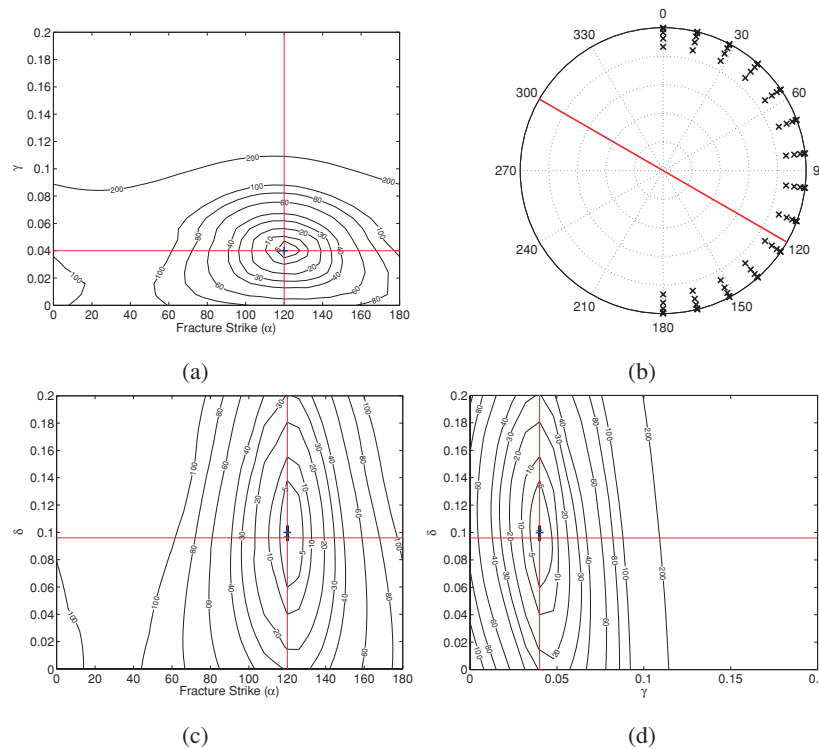


Figure 2. Inversion results for the first synthetic example, with subhorizontal arrivals. A stereoplot of arrivals is shown in (b) along with the strike of the vertical fracture set. The normalized misfit contours as a function of α , γ and δ are plotted at the best-fitting value of ξ . In (a) γ and α are plotted at best-fitting δ , in (c) α and δ are plotted at best-fitting γ , and in (d) γ and δ at best-fitting α . The blue crosses mark the initial values used to generate the synthetic data ($\gamma = 0.04$, $\delta = 0.1$, $\alpha = 120^\circ$ and $\xi = 0.04$) and the red lines indicate the inversion results. The misfit contours are normalized such that 1 is the 90 per cent confidence limit. In this case, γ and α are well constrained, whilst δ is not.

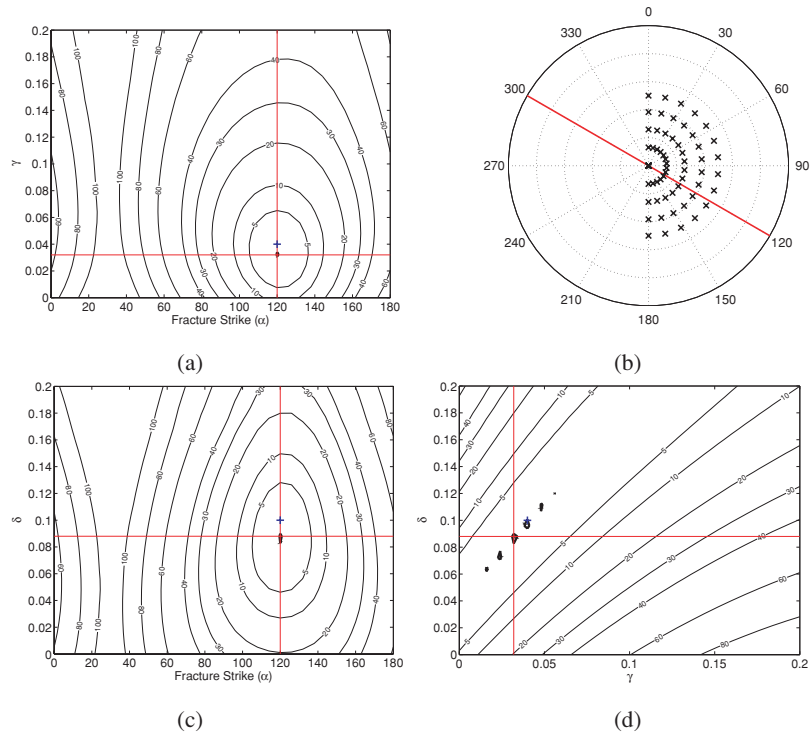


Figure 3. Inversion results for the second synthetic example, with subvertical arrivals, in the same format as Fig. 2. The initial elastic model is also the same. In this case, there is a trade-off between γ and δ , meaning that neither is well constrained.

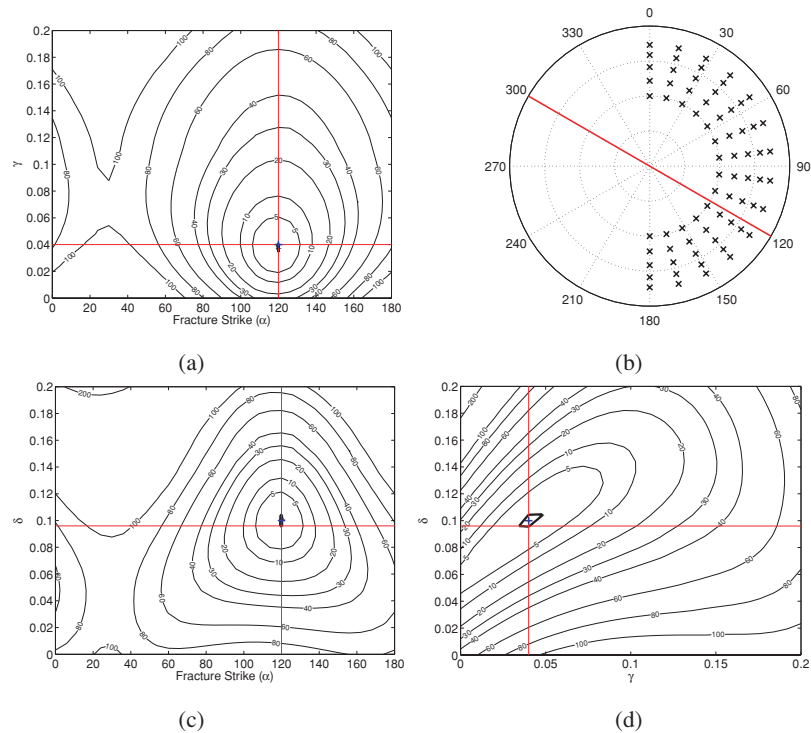


Figure 4. Inversion results for the third synthetic example, with oblique arrivals, in the same format as Fig. 2. The initial elastic model is still the same. There is still some trade-off between γ and δ , but both are better constrained than in Fig. 3.

variation in δ does not significantly affect the inversion. Hence for the following examples we do not plot δ , but plot the misfit as a function of γ , α and ξ at the best-fitting value of δ . The first model we consider has no fractures, only a VTI fabric with $\gamma = 0.04$.

The results are shown in Fig. 5; the inversion accurately identifies the lack of fractures and determines γ satisfactorily. We contrast this with a model containing fractures striking at $\alpha = 120^\circ$ with a density of $\xi = 0.08$. In this case, the waves propagate in directions

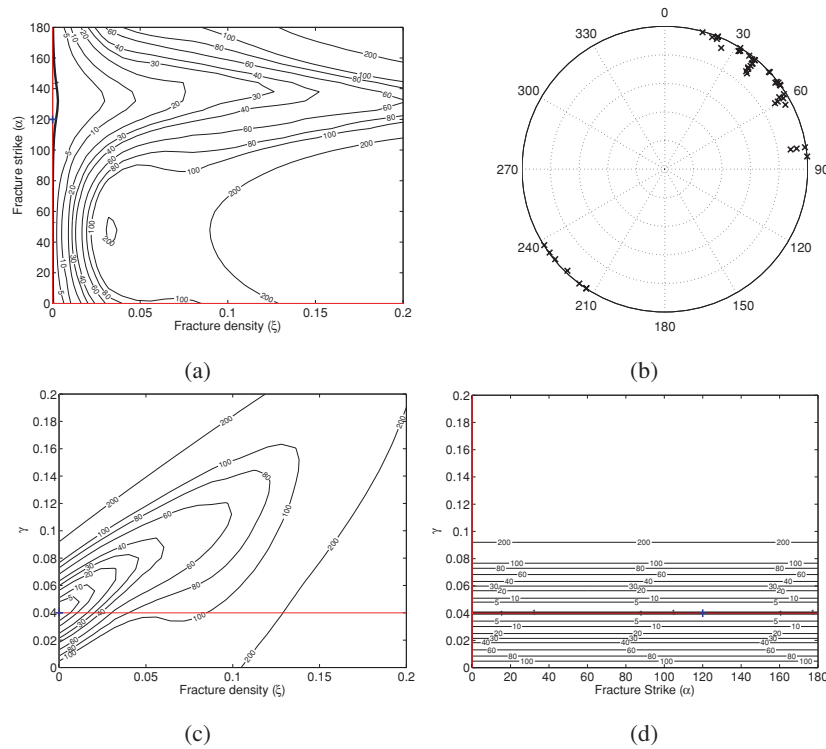


Figure 5. Inversion results for the fourth synthetic example. This case uses the arrivals from the real data, which are subhorizontal. The initial elastic model has $\gamma = 0.04$ and $\delta = 0.1$, with no fractures present ($\xi = 0$). As the inversion is not sensitive to δ , we plot the misfit contours as a function of γ , α and ξ . The inversion accurately identifies γ and the lack of fractures.

close to the fracture normals. The results are shown in Fig. 6. The inversion accurately identifies the fracture strike and VTI fabric strength. Fracture density is constrained to some extent, but not as accurately as for the other parameters. The limitation that for this geometry of ray paths and fractures it is difficult to constrain fracture density should be remembered when we come to look at the real data set.

To further test how well imaged the fracture strike is for this geometry, we construct a final synthetic test, with the same range of arrivals, but fractures now striking at 90° which is 30° away from the strike used in the previous model. The results, in Fig. 6, show that the differences in fracture strike between this and Fig. 5 have been correctly identified. Furthermore, the uncertainty in ξ appears to have been reduced compared to Fig. 6. We suggest that this is because the waves have travelled at a more oblique angle to the fractures, and so are affected by them more significantly.

This section does not intend to cover every possible source–receiver geometry, these will obviously be specific to the problem being investigated. However, we have outlined how synthetic modelling can guide the interpretation of SWS results, and highlight what real data is likely to identify, and what it cannot. For instance, from Fig. 6 we anticipate that our data set will be able to constrain fracture strike but not the fracture density. Furthermore, synthetic modelling can highlight ways to improve the effectiveness of the inversion. For instance, from Fig. 7 we suggest that had the geophones been placed such that the shear waves had travelled closer to the fracture strike (if only by a 30° difference) then it would be much easier to image the fracture density. This capacity may be of use to field engineers when selecting sites to place geophones.

4 APPLICATION TO A PASSIVE SEISMIC DATA SET

4.1 Field description

In order to demonstrate this approach with real data, we consider a typical passive seismic monitoring data set from a hydraulic fracture stimulation. A water-based gel was used as the injected fluid, and the fracture development was monitored on an array of 12 3-C geophones located in a vertical well a short distance from the injection well. 65 reliable events were located using P -wave hodograms and P - S traveltimes differences following the method outlined in Zimmer *et al.* (2007). The dominant frequencies of the recorded energy ranged from 100 to 150 Hz. The locations of the events (with 95 per cent confidence limits) are plotted in Fig. 8, and they are seen to map the formation of fractures extending to the NW and SE of the injector at $\sim 120^\circ$. The source–receiver ray paths are predominately subhorizontal, and do not travel outside the reservoir rocks. Therefore, we do not anticipate significant variations in anisotropy along or between ray paths.

The SWS parameters, ψ and δV_S , were measured for each shear wave arrival at each receiver using the semi-automated covariance matrix minimization approach of Teanby *et al.* (2004b). Of the 780 potential splitting measurements (65 events \times 12 receivers) 45 were deemed to be of the top class following the quality control steps outlined by Teanby *et al.* (2004b). This is a typical success rate for a microseismic data set (e.g. Teanby *et al.* 2004a). A horizontal projection of the splitting measurements is plotted in Fig. 9 showing ψ and δV_S as a function of arrival θ and ϕ . This is the data set that we invert for fracture properties.

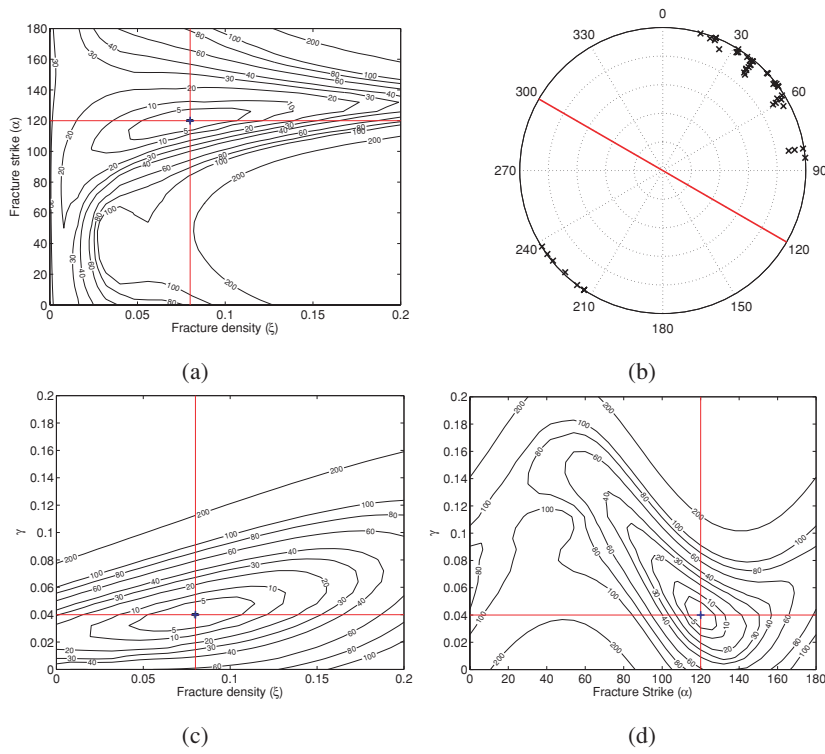


Figure 6. Inversion results for the fifth synthetic example, in the same format as Fig. 5. This case also has subhorizontal arrivals, but with fractures striking at 120° ($\gamma = 0.04, \delta = 0.1, \xi = 0.08$ and $\alpha = 120^\circ$). The inversion accurately identifies γ and the fracture strike, but fracture density is only poorly constrained.

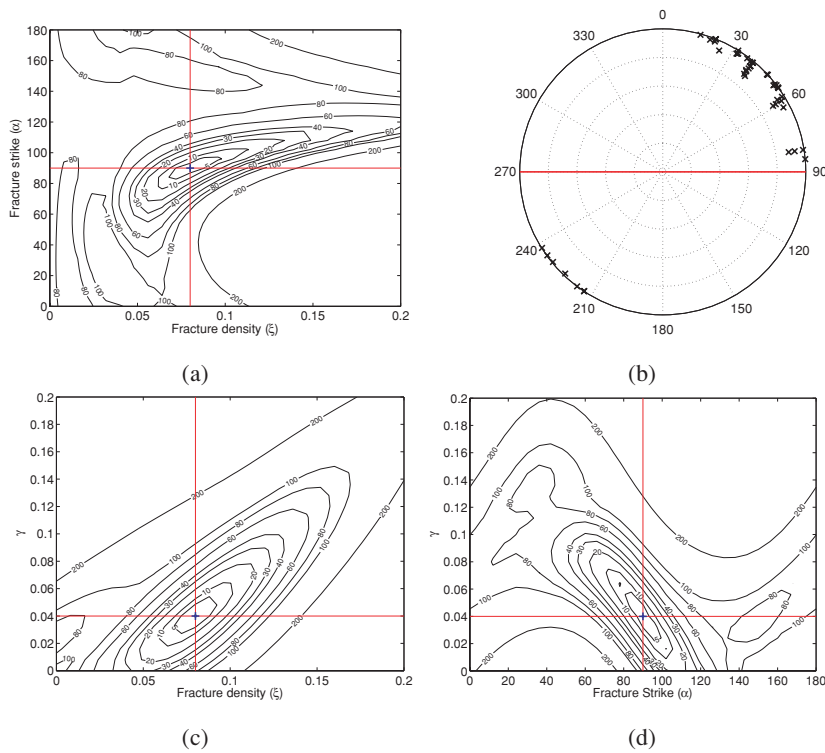


Figure 7. Inversion results for the sixth synthetic example, in the same format as Fig. 5. This case also has subhorizontal arrivals, but with fractures striking at 90° ($\gamma = 0.04, \delta = 0.1, \xi = 0.08$ and $\alpha = 90^\circ$). As the waves have travelled more obliquely to the fractures, fracture density is better constrained than in Fig. 6.

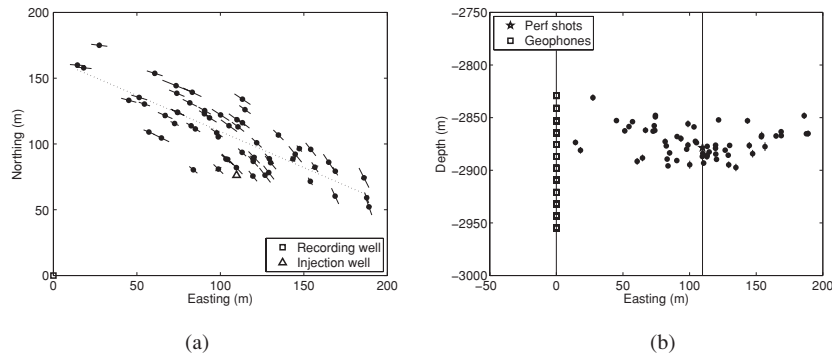


Figure 8. Locations of microseismic events induced by fracture stimulation. (a) shows a map view: the vertical recording well is at (0,0), the injection well is marked. (b) shows a side view: the geophones and perforation depths are plotted. Error bars represent the 95 per cent confidence interval. The events form a trend running at $\sim 120^\circ$ from the injection well.

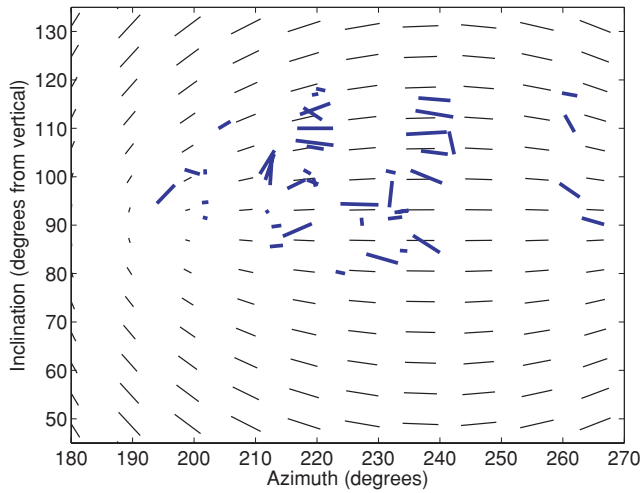


Figure 9. Cylindrical projection of splitting results for the passive seismic data set (in blue). Tick orientations indicate ψ (i.e. parallel to the y -axis represents a vertical polarization) and tick lengths represent δV_S . Also plotted (in black) are the results for the model that best fits the data.

4.2 Results

The results of the inversion for this data set are plotted in Fig. 10. We note that as anticipated from the inversions with synthetic data, the fracture strike and VTI fabric are well imaged (with $\alpha = 120^\circ \pm 12^\circ$ and $\gamma = 0.040 \pm 0.005$) whilst the fracture density is not well constrained. As an independent measure of fracture strike, the event locations suggest the formation of fractures trending at approximately 120° from the injection well. The match between fracture strike estimated from event locations and independently from SWS indicates the success of the inversion. We do not have an independent estimate for γ , however the value obtained is well within the reasonable bounds for sedimentary rocks in hydrocarbon settings ($\gamma \approx 0-0.2$ for sandstones, Thomsen 1986). We plot the splitting predicted by the best-fitting model in Fig. 9, and we note a good match between our model and the observed splitting.

5 DISCUSSION

When interpreting SWS caused by fractures, it is commonly assumed that the fast direction rotated into geographical coordinates corresponds to the strike of the major fracture set and/or the maximum horizontal principal stress orientation, and that an increase

in δV_S corresponds to an increase in fracture density. However, in reality, this may be an oversimplification. The presence of fractures, sedimentary layering and other structures all combine to give the overall elasticity of a rock. The respective contributions must all be understood before SWS can be interpreted with confidence. For instance, in this data set the maximum splitting is observed when waves travel normal to the fractures, that is, in a direction where the waves would not be split by the fractures. The effect of the fractures is to cancel the anisotropy caused by the VTI fabric, and it is notable that for certain directions of shear wave propagation models with lower fracture densities predict higher δV_S than models with a high fracture density. This highlights the need to consider all the potential contributions to anisotropy when interpreting SWS. It also demonstrates how detailed modelling can be used to infer fracture properties despite an unfavourable source-receiver geometry.

As mentioned above, we invert for an orthorhombic symmetry assuming a single set of vertical fractures and a VTI fabric, and the model we use to estimate the fracture compliance is quite simple. These assumptions were made in order to reduce the number of free parameters and therefore simplify the inversion, while being appropriate for the reservoir analysed. They are not necessary conditions. We could certainly conceive of situations where additional fracture sets, dipping fractures or dipping sedimentary structures, or more complex fracture models, might be preferred, particularly if there were *a priori* evidence to suggest their existence in a reservoir. This would increase the number of free parameters and therefore increase the complexity (and computational requirements) of the inversion. However, this may be appropriate under certain circumstances.

6 CONCLUSIONS

We have outlined a method for inverting for fracture and sedimentary fabric properties using shear wave splitting measured on seismic waves recorded from microseismic events. Interpreting such shear wave splitting measurements, which will have a range of arrival angles, is non-trivial. We use rock physics theory to model the elastic anisotropy of likely subsurface structure, allowing us to predict the SWS of a wave propagating in any direction. This allows us to find the best-fitting model that matches SWS observations.

We generate synthetic data to test the inversion approach, finding that the success of the inversion is highly sensitive to the ray coverage, as well as the orientation of the ray coverage with respect to subsurface structures, in a manner that is often non-intuitive. This synthetic approach allows us to identify in advance the likelihood that SWS measurements with a certain ray coverage will allow us

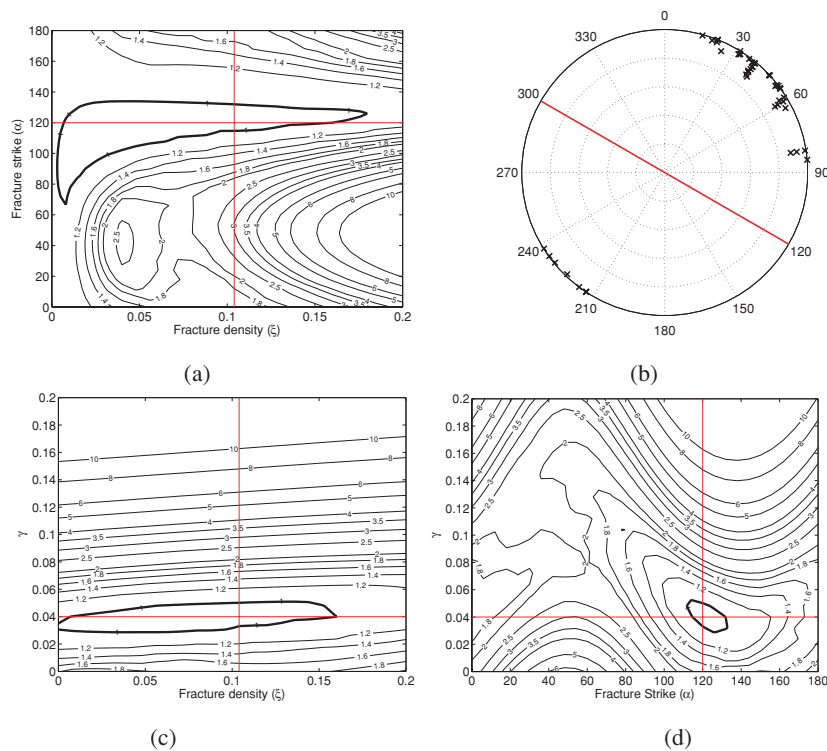


Figure 10. Inversion results for the passive seismic data set, in the same format as Fig. 5. The 90 per cent confidence interval is marked in bold. The inversion has accurately determined the fracture strike and sedimentary fabric strength. As anticipated from the synthetic tests, the fracture density is poorly imaged.

to constrain the structure, and could potentially be used as a guide in deciding the optimum receiver geometry if SWS is to be used as an effective tool.

We have demonstrated this technique on a passive seismic data set from a hydraulic fracture stimulation. The inversion results for the fracture strike agree with independent estimates from event locations, whilst, as anticipated from synthetic modelling, we were not able to constrain the fracture density accurately.

ACKNOWLEDGMENTS

We would like to thank Pinnacle Technologies for making the passive seismic data available, and Shawn Maxwell and Natalia Verkhovtseva for their help in the initial processing. We would also like to thank GJI associate editor Johan Robertsson, and Mark Chapman and the anonymous reviewers whose comments substantially improved the paper. Discussions with V. Grechka on fractures set in VTI media were also very helpful. James Verdon was funded by a UKERC Interdisciplinary Studentship.

REFERENCES

- Abt, D.L. & Fischer, K.M., 2008. Resolving three-dimensional anisotropic structure with shear wave splitting tomography, *Geophys. J. Int.*, **173**(3), 859–886.
- Backus, G.E., 1962. Long-wave elastic anisotropy produced by horizontal layering, *J. geophys. Res.*, **66**, 4427–4440.
- Crampin, S. & Peacock, S., 2008. A review of the current understanding of seismic shear-wave splitting in the earth's crust and common fallacies in interpretation, *Wave Motion*, **45**, 675–722.
- Grechka, V., 2007. Multiple cracks in VTI rocks: effective properties and fracture characterisation, *Geophysics*, **72**(5), D81–D91.

- Hall, S.A. & Kendall, J.-M., 2000. Constraining the interpretation of AVOA for fracture characterisation, in *Anisotropy 2000: Fractures, Converted Waves, and Case Studies*, pp. 107–144, eds Ikelle, L. & Gangi, A., Society of Exploration Geophysics, Tulsa, OK.
- Hall, S.A., Kendall, J.-M., Maddock, J. & Fisher, Q., 2008. Crack density tensor inversion for analysis of changes in rock frame architecture, *Geophys. J. Int.*, **173**, 577–592.
- Horne, S. & MacBeth, C., 1994. Inversion for seismic anisotropy using genetic algorithms, *Geophys. Prospect.*, **42**, 953–974.
- Hudson, J., 1981. Wave speeds and attenuation of elastic waves in material containing cracks, *Geophys. J. R. astr. Soc.*, **64**, 133–150.
- Hudson, J.A., Liu, E. & Crampin, S., 1996. The mechanical properties of materials with interconnected cracks and pores, *Geophys. J. Int.*, **124**, 105–112.
- Kendall, J.-M. *et al.*, 2007. Seismic anisotropy as an indicator of reservoir quality of siliclastic rocks, in *Structurally Complex Reservoirs*, pp. 123–136, eds Jolley, S., Barr, D., Walsh, J. & Knipe, R., Geological Society of London Special Publication.
- Pointer, T., Liu, E. & Hudson, J.A., 2000. Seismic wave propagation in cracked porous media, *Geophys. J. Int.*, **142**, 199–231.
- Rial, J.A., Elkibbi, M. & Yang, M., 2005. Shear-wave splitting as a tool for the characterization of geothermal fractured reservoirs: lessons learned, *Geothermics*, **34**, 365–385.
- Schoenberg, M. & Sayers, C.M., 1995. Seismic anisotropy of fractured rock, *Geophysics*, **60**(1), 204–211.
- Silver, P.G. & Chan, W.W.J., 1991. Shear-wave splitting and subcontinental mantle deformation, *J. geophys. Res.*, **96**, 16 429–16 454.
- Teanby, N., Kendall, J.-M., Jones, R.H. & Barkved, O., 2004a. Stress-induced temporal variations in seismic anisotropy observed in micro-seismic data, *Geophys. J. Int.*, **156**, 459–466.
- Teanby, N., Kendall, J.-M. & van der Baan, M., 2004b. Automation of shear-wave splitting measurements using cluster analysis, *Bull. seism. Soc. Am.*, **94**(2), 453–463.
- Thomsen, L., 1986. Weak elastic anisotropy, *Geophysics*, **51**(10), 1954–1966.

- Valcke, S.L.A., Casey, M., Lloyd, G.E., Kendall, J.-M. & Fisher, Q.J., 2006. Lattice preferred orientation and seismic anisotropy in sedimentary rocks, *Geophys. J. Int.*, **166**, 652–666.
- Verdon, J.P., Angus, D.A., Kendall, J.-M. & Hall, S.A., 2008. The effects of microstructure and nonlinear stress on anisotropic seismic velocities, *Geophysics*, **73**(4), D41–D51.
- Wooley, J., 2009. Direct probabilistic inversion of shear-wave data for anisotropy, *Presented at the Frontiers of Seismology Conference*, BGS and University of Edinburgh.
- Wüstefeld, A., 2007. Null detection in shear-wave splitting measurements, *Bull. seism. Soc. Am.*, **97**(4), 1204–1211.
- Zatsepin, S. & Crampin, S., 1997. Modelling the compliance of crustal rock-I. Response of shear-wave splitting to differential stress, *Geophys. J. Int.*, **129**, 477–494.
- Zimmer, U., Maxwell, S., Waltman, C. & Warpinski, N., 2007. Microseismic monitoring quality-control (QC) reports as an interpretative tool for nonspecialists, SPE 110517, *Presented at the SPE Annual Technical Conference*, Anaheim, CA, Society of Petroleum Engineers (SPE), Richardson, TX.